Nonlinear surface impedance for $YBa_2Cu_3O_{7-x}$ thin films: Measurements and a coupled-grain model

P. P. Nguyen
Department of Physics, Massachusetts Institute of Technology, Cambridge, Massachusetts 02139 and Rome Laboratory, Hanscom Air Force Base, Massachusetts 01731

D. E. Oates
Lincoln Laboratory, Massachusetts Institute of Technology, Lexington, Massachusetts 02173

G. Dresselhaus
Francis Bitter Magnet Laboratory, Massachusetts Institute of Technology, Cambridge, Massachusetts 02139 and Rome Laboratory, Hanscom Air Force Base, Massachusetts 01731

M. S. Dresselhaus
Department of Electrical Engineering and Computer Science and Department of Physics, Massachusetts Institute of Technology, Cambridge, Massachusetts 02139
(Received 16 April 1993)

We present measurements of the surface impedance as a function of frequency (1–17 GHz), temperature (4.2–91 K), and peak rf magnetic field ($0 < H_{rf} < 500$ Oe) for high-quality epitaxial $YBa_2Cu_3O_{7-x}$ thin films using a stripline-resonator technique. The lowest surface resistance at 1.5 GHz was 15 $\mu\Omega$ at 77 K and 3 $\mu\Omega$ at 4.3 K. The results for the low- and intermediate-field regions ($H_{rf} < 50$ Oe at 77 K) are explained by a coupled-grain model, which treats the film as a network of superconducting grains connected by grain boundaries acting as resistively shunted Josephson junctions. Quantitative agreement has been obtained between the model and the measurements. The effective junction critical current density, grain size, and shunt resistance are used in the model to characterize the films. The high-field region may be explained by flux penetration into the grains but is not modeled in detail here.

I. INTRODUCTION

Microwave measurements of the surface impedance $Z_s = R_s + jX_s$, where R_s is the surface resistance and X_s the surface reactance, provide one of the most useful probes of the superconducting state. The surface resistance R_s results from microwave power losses and can be related to the normal carrier density, whereas X_s reveals information about the superconducting electron density. Z_s is a material parameter and is defined as the ratio of the electric field at the surface to the surface current density of a semi-infinite half-space homogeneous conductor.

This paper is concerned with measurements and modeling of Z_s as a function of temperature, frequency, and rf magnetic field of high-quality $YBa_2Cu_3O_{7-x}$ thin films in order to provide insight into the mechanisms of superconductivity and to better understand the microwave properties when the films are applied to practical devices.

The surface resistance R_s in epitaxial thin films of high-temperature superconductors deviates considerably from the predicted BCS exponential drop at low temperature[1] below the superconducting transition temperature T_c. The difference between the measured R_s and that calculated from the BCS theory is defined as the residual surface resistance, which is in part the subject of this paper. All superconductors show a finite residual surface resistance which dominates the intrinsic BCS value at sufficiently low temperatures. In the oxide high-T_c materials, however, the residual surface resistance is dominant up to $t = T/T_c = 0.9$. As will be discussed below, our analysis and measurements are consistent with the residual surface resistance being an extrinsic effect, resulting from defects in the material.

The nonlinearity in Z_s, i.e., the dependence of Z_s on the microwave current I_{rf}, in the oxide superconductors has been observed by a number of workers in both bulk and thin film materials.[2–4] Nonlinear effects provide a means to study the pair-breaking process, vortex creation, and vortex motion. A better understanding of the nonlinearity can also help high-T_c film makers characterize and improve their films. The strong power dependence of Z_s in high-temperature superconductors invariably affects possible applications of these materials. Decreases in the resonant Q or increases in device loss have a negative impact on device performance. Moreover, a nonlinear impedance leads to such nonlinear effects as intermodulation distortion and harmonic generation. Microwave frequency $1/f$ noise may also be related to nonlinear conduction processes.

In this paper we attempt to model the linear (in the limit of zero rf field) surface impedance as well as the

0163-1829/93/48(9)/6400(13)/$06.00

nonlinear effects in one self-consistent model. The linear residual surface resistance has also been an important subject for study in high-T_c materials, and a number of authors have proposed models to explain it.[5–9] The nonlinear effects have also been measured by a variety of workers.[3,4,10] Little work, however, has been done to date to model the nonlinear effects in epitaxial films. The epitaxial films reported here show similar behavior from sample to sample and therefore can be modeled in a consistent manner.

A preliminary report of our experimental results[2] discussed the possibility that the Ginzburg-Landau (GL) theory could be used to explain them. It was shown[2] that the functional dependence of $R_s(T)$ on rf power was consistent with the GL theory. Lam *et al.*[11] have also shown that the GL theory can be used to fit the change in the resonant frequencies. Further efforts to calculate quantitatively the power dependence of $R_s(T)$ using the GL theory have shown that the power-induced change in $R_s(T)$ deduced from our measurements is too large to be explained by the GL theory with a reasonable value of the thermodynamic critical field H_c.[12] In addition, even with an extremely low H_c (< 0.1 T at 0 K), the GL theory fails to simultaneously fit the power dependences of both R_s and the resonant frequencies with the same parameters. As will be seen later, the coupled-grain model developed in this paper agrees quantitatively with our measurements and can fit simultaneously both R_s and the resonant frequencies with the same parameters.

The coupled-grain model presented here is based on the film being composed of a network of superconducting grains connected by grain-boundary weak links acting as resistively shunted Josephson junctions. The grains are modeled as having intrinsic properties which can be calculated from the BCS and the Ginzburg-Landau theories. The properties of the grain boundaries are extrinsic to those of the grains. The residual R_s and the nonlinear part of R_s are related to the properties of the grain boundaries which dominate over those of the grains for temperatures $T/T_c < 0.9$. The magnetic penetration depth λ contains information on both the grains (i.e., the energy gap) and the grain boundaries (i.e., the junction critical current density and the shunt resistance). Physically, the grain boundaries determine the resistance because they are in series with the very small intrinsic resistance of the grains at low temperature. The grains, however, determine much of the inductance of the film (and hence the current distribution), since they constitute most of the volume of the material. This simple physical picture explains why the measured penetration depth is close to its intrinsic value, while the surface resistance is orders of magnitude larger than its intrinsic value at low temperatures.

This paper is organized as follows: Section II describes our experimental techniques and defines the parameters to be used later. Section III presents our data on R_s and λ in both the linear and nonlinear regimes. Section IV develops a coupled-grain model to explain the data. In Sec. V, reasonable parameters are substituted into the model and the results are then compared with the measurements. Section VI is the summary.

II. EXPERIMENTAL TECHNIQUES

A stripline resonator technique was used to measure the surface impedance of $YBa_2Cu_3O_{7-x}$ thin films. The experimental method and device fabrication have been described previously.[13] Figure 1 shows the cross section and the top view of the resonator. At resonance, the induced rf current forms sinusoidal standing waves of wavelength $2l/n$ along the length l of the conductors (z direction) where $n = 1, 2, \ldots$ is the mode number.

In this study, several $YBa_2Cu_3O_{7-x}$ films have been measured. Some characterization parameters for four films with the lowest zero rf field surface resistance and the weakest rf field dependence are tabulated in Table I. The superconducting transition temperatures T_c were determined from rf measurements, and the critical current densities J_c^T for films deposited under the same conditions were obtained by dc transport measurements. The zero-temperature penetration depth $\lambda(0\text{ K})$ was estimated from the temperature dependence of the resonant frequencies.[14]

The films were deposited by off-axis *in situ* sputtering onto $LaAlO_3$ substrates.[15] They have high superconducting transition temperatures (between 86 and 90 K), narrow transition widths (less than 0.5 K), and dc critical current densities that exceed 10^7 A/cm^2 at 4.2 K and 10^6 A/cm^2 at 77 K.[15] The low-field surface resistance is comparable to that of other high-quality films reported in the literature.[1]

To measure the nonlinear surface impedance $Z_s(H_{rf})$, where H_{rf} is the peak surface magnetic field generated by the rf current, H_{rf} is varied by changing the input power to the resonator and measuring Q and the resonant frequency f_0 as a function of power level. R_s and X_s are derived from Q and f_0, respectively, and H_{rf} is calculated from I_{rf} as described later. Here $X_s = j\omega\mu_0\lambda$ where $\omega = 2\pi f$, f is the frequency, and μ_0 the permeability of free space.

At low power, the resonant curve is Lorentzian in shape, and Q is given by $f_0/\delta f_0$, where δf_0 is the 3-dB bandwidth. As the power is increased, the resonant curve deviates from the Lorentzian line shape.[2] When the resonant curve gets distorted, the calculation of Q by the 3-dB bandwidth criterion becomes invalid. An equiva-

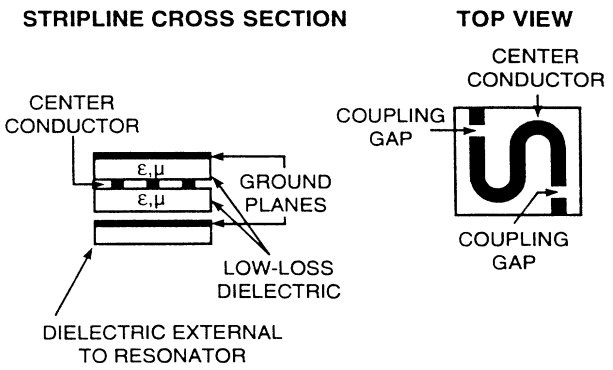

FIG. 1. Stripline resonator.

TABLE I. Parameters of the $YBa_2Cu_3O_{7-x}$ films measured.

	Film 1	Film 2	Film 3	Film 4
Thickness d (μm)	0.3	0.3	0.3	0.3
T_c (K)	86.4	89.5	89.6	90.0
$\lambda(0\ \mathrm{K})$ (μm)	0.17	0.22	0.27	0.20
$J_c^T(4.3\ \mathrm{K})$ (A/cm^2)	$>10^7$	$>10^7$	$>10^7$	$>10^7$

lent circuit can be used to show that Q is proportional to the insertion loss at the peak of the resonant curve.[16] In practice, however, the Q values measured by the 3-dB points and by the insertion loss at the resonant peak are found to differ by less than 10%. Consequently, we used the 3-dB bandwidth criterion to calculate Q in this paper. The resonant frequency for the non-Lorentzian resonant curve is still at the peak of the curve, where the total reactance of the circuit is zero. The shape of the non-Lorentzian curves, which is typical of a nonlinear oscillator, has been modeled quantitatively by Oates *et al.*,[17] whose results are in excellent agreement with the experimental data.

As is the case for any transmission-line geometry, in the cross-sectional xy plane of the superconducting stripline, the rf current density peaks at the surfaces, edges, and corners.[14] For the superconducting Y-Ba-Cu-O stripline in the frequency range that was considered in this work ($1 < f < 17$ GHz), the Meissner effect dominates over the classical skin-depth effect in determining the depth of the rf field penetration. At 77 K and 1 GHz, by taking the normal resistivity ρ_n to be 50 $\mu\Omega$ cm, the skin depth is estimated to be 11.4 μm, which is much larger than the effective magnetic penetration depth ($\lambda \sim 0.2$ μm). The scale of the rf current peaks in the cross-sectional xy plane of Fig. 1 is hence determined by λ (except at temperatures very close to T_c, which are not considered here, where λ exceeds the skin depth).

From the input power and insertion loss, we can calculate the rf current in the standing waves at resonance. As derived in Ref. 18 for the limit of zero rf current (the linear case), the peak current I_0 at the maxima of the standing wave is given by

$$I_0 = \sqrt{\frac{r_v(1-r_v)8Q_cP}{n\pi Z_0}}, \tag{1}$$

where r_v is the voltage insertion ratio, related to the insertion loss IL by $\mathrm{IL} = -20\ln r_v$, Q_c is the unloaded Q of the stripline resonator which can be calculated from the measured loaded Q and the IL, P is the incident power, n is the resonant mode number, and Z_0 is the characteristic impedance of the stripline. The current as a function of the position z along the length of the stripline is

$$I_{\mathrm{rf}}(z,t) = I_0 \sin\left(\frac{n\pi z}{l}\right)\cos(\omega t), \tag{2}$$

where l is the length of the resonator center line and $\omega = 2\pi f$ with f being the frequency. Though derived assuming a linear circuit, Eqs. (1) and (2) will be used to calculate the current at high rf power because, as presented in Sec. III, the measurements show that the changes in the total inductance of the transmission line are small, even at the highest rf power levels considered in this paper. Therefore, the total current and the current distribution remain, to a good approximation, unchanged at high power, since they are determined by the inductance.

In the limit of zero rf field, $\lambda(T)$ has been evaluated[13,14] from the temperature dependence of the resonant frequencies, assuming the two-fluid model temperature dependence $\lambda(T) = \lambda(0)/\sqrt{1-(T/T_c)^4}$ with T_c and $\lambda(0)$ the fitting parameters. The values for $\lambda(0)$ determined this way (see Table I) are comparable to values found by others.[8,10,19] The calculated $\lambda(0)$ is sensitive to both T_c and the assumed temperature dependence of $\lambda(T)$, and hence can have a systematic error of up to 20%.

Similarly, in the limit of zero rf field, R_s, defined as the real part of the ratio of the surface electric field to the surface current density for a semi-infinite half-space conductor, can be obtained from Q_c, the unloaded Q,[13] by

$$R_s = \Gamma[\lambda(T)/d]f/Q_c, \tag{3}$$

where $\Gamma[\lambda(T)/d]$ is the geometrical factor for a stripline of film thickness d and effective London penetration depth $\lambda(T)$. Given a (uniform) effective complex resistivity ρ, the surface resistance R_s is related to ρ by

$$R_s = \mathrm{Re}(Z_s) = \mathrm{Re}[(j\omega\mu_0\rho)^{1/2}]. \tag{4}$$

Throughout this paper we present the surface impedance data as a function of H_{rf}, defined as the peak rf field at the edges of the center conductor of the stripline and at the peaks of the standing-wave maxima at resonance. The field H_{rf} can be calculated from the current distribution[14] after using Eq. (1) to obtain the peak current I_0. In the limit of zero rf field, H_{rf} is proportional to I_0, and the proportionality constant is a function of the geometry and $\lambda(T)$. At finite rf field, the proportionality constant becomes dependent also on I_{rf}. For the low- and intermediate-field regions (the vortex-free regions), we can use the zero-field value for the proportionality constant since the power dependence of this constant is weak.[11] For the high-field region, which is not discussed in detail in this paper, our estimate yields only an upper limit to the true H_{rf}.

For rf fields at which nonlinear effects become observable, the power dependence of the geometrical factor Γ in Eq. (3) must be taken into account. Furthermore, Eq. (4) no longer holds, since the bulk resistivity ρ becomes spatially nonuniform. Nevertheless, we define an effective surface resistance as

$$R_s \equiv \Gamma[\lambda(T)/d]f/Q_c, \tag{5}$$

which reduces to Eq. (4) if ρ is spatially uniform. (In the low- and intermediate-field regimes considered in this paper, ρ is in fact fairly uniform, as we shall see in Sec. IV.) This is the definition for R_s that we use throughout the

paper. Note $\Gamma[\lambda(T)/d]$ here is the geometrical factor in the zero-field limit (assumed to be independent of rf power).

Analogously, the effective London penetration depth λ, which is inversely proportional to the superconducting carrier density, becomes spatially nonuniform for nonzero rf fields. We define, however, an effective λ as follows:

$$\lambda(T, H_{\rm rf}) \equiv F[f_0(T, H_{\rm rf})], \tag{6}$$

where $F[f_0(T, H_{\rm rf})]$ is the function mapping the temperature-dependent $f_0(T, 0)$ into $\lambda(T, 0)$ in the zero-field limit.[14] Recall that f_0 denotes the resonant frequency (of a certain mode n) of the resonator, whereas f denotes the frequency. The field-induced change $\Delta\lambda(T, H_{\rm rf})$ can be calculated using

$$\frac{\Delta\lambda(T, H_{\rm rf})}{\lambda} = -\frac{2L}{\lambda dL/d\lambda}\frac{\Delta f_0(T, H_{\rm rf})}{f_0}, \tag{7}$$

where L is the total inductance of the stripline resonator, and $dL/d\lambda$ is its derivative with respect to λ.[14]

III. EXPERIMENTAL RESULTS

A. Zero rf field limit

We define the zero-field limit for $H_{\rm rf}$ as the value of $H_{\rm rf}$ below which $R_s(H_{\rm rf})$ is essentially independent of $H_{\rm rf}$. For all of the striplines reported here, $H_{\rm rf} \leq 0.5$ Oe satisfies this definition. Experimentally, we find that the behavior of R_s is dominated by the residual surface resistance at low temperature ($T/T_c < 0.9$) and the BCS theory does not apply. Figure 2 shows the zero field R_s vs the reduced temperature $t = T/T_c$ for resonators 1 (circles), 2 (asterisks), and 4 (triangles). At 1.5 GHz, the lowest R_s value is 15 $\mu\Omega$ at 77 K and 3 $\mu\Omega$ at 4.3 K. These films show the typical R_s vs T behavior. As observed also by others,[1,3] R_s drops sharply near T_c but then levels off to become nearly independent of T at low T, instead of decreasing exponentially to zero for $T \to 0$ as predicted by the BCS calculations. The high values of $R_s(T \to 0)$ for high-temperature superconductors are probably nonintrinsic since these values vary from sample to sample (Fig. 2) and sometimes even within the same samples over time.[10]

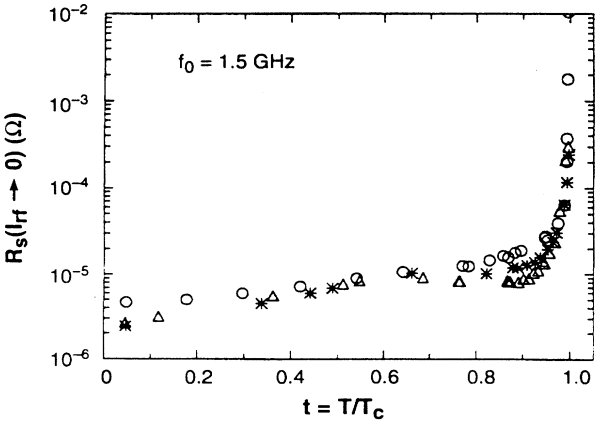

FIG. 2. Zero field R_s for resonator 1 (circles), 2 (asterisks), and 4 (triangles) as a function of the reduced temperature $t = T/T_c$. See Table I for the parameters of the films.

The small local maxima in the $R_s(t)$ curves around the reduced temperature $t \approx 0.6$ are less prominent for resonator 1 than for the other two. Other workers[10,20] have observed similar peaks in R_s, although the temperature at which these peaks occur and the values of their heights appear sample dependent. The significance of the peaks is not yet well understood.

B. rf field dependence

All the rf field dependence data presented in this section come from resonator 1. Equivalent measurements on resonators 2 and 3 show similar behavior. Figure 3 shows a typical set of values for the measured R_s and λ as functions of $H_{\rm rf}$. The solid lines are least-squares fits of the data to the functions

$$R_s = R_s(0)[1 + b_R H_{\rm rf}^2] \tag{8}$$

and

$$\lambda = \lambda(0)[1 + b_\lambda H_{\rm rf}^2], \tag{9}$$

respectively, for $H_{\rm rf} < H_p$, where b_R and b_λ are fitting constants. We define H_p to be the field below which both curves exhibit quadratic dependences on $H_{\rm rf}$. This quadratic behavior is explained by the coupled-grain model introduced in Sec. IV. We determine H_p by the fol-

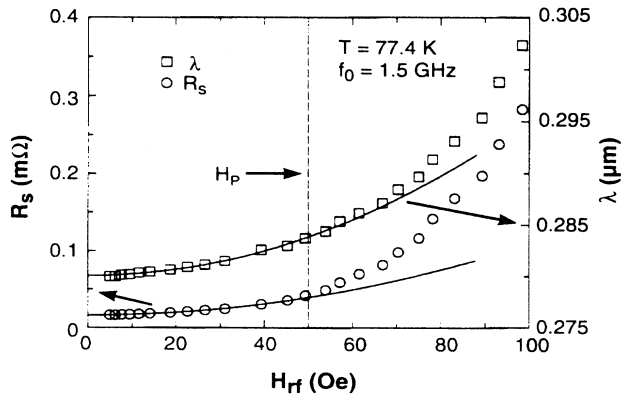

FIG. 3. A typical set of data for the surface resistance R_s (circles) and the penetration depth λ (squares) vs $H_{\rm rf}$. These data are for $T = 77.4$ K and $f_0 = 1.5$ GHz. The dashed line separates the vortex-free (left) region from the vortex-penetration (right) region. The circles refer to the left-hand scale and the squares to the right-hand scale. The solid lines are the best least-squares fits to the quadratic functions $R_s = R_s(0)[1 + b_R H_{\rm rf}^2]$ and $\lambda = \lambda(0)[1 + b_\lambda H_{\rm rf}^2]$ for the circles and squares, respectively, where $R_s(0)$ and $\lambda(0)$ denote the zero-field values, and b_R and b_λ are fitting constants.

lowing procedure. First, we plot R_s as a function of H_{rf}^2. In the low- and intermediate-field regions, the data follow a straight line since R_s varies quadratically with H_{rf}. Second, we fit a straight line through this low and intermediate region. The field point above which the data deviate by more than some threshhold value is defined to be H_p. In Fig. 3, the threshhold value is $5 \times 10^{-6}\Omega$ at 77.4 K and 1.5 GHz, giving $H_p \approx 50$ Oe. The parameters b_R and b_λ [in Eqs. (8) and (9)] are important for comparisons with the coupled-grain model discussed in Sec. IV of this paper. We have found that b_R and b_λ do not depend very strongly on the exact choice of the value of H_p. For example, for the case of the data shown in Fig. 3, b_R and b_λ vary by less than 5% for values of H_p smaller than 50 Oe. This insensitivity of b_R and b_λ to the choice of H_p is typical of the data at all temperatures and frequencies. Thus, as will be seen later, our conclusions are not at all dependent on the value of H_p. Above H_p, R_s increases faster than H_{rf}^2.

Figure 4 presents the unloaded Q vs H_{rf} for resonator 1 at 77.4 K for the two lowest resonant modes $n = 1$ at 1.5 GHz and $n = 2$ at 3.1 GHz. From the figure, we see that for the low- and intermediate-field regions, Q is approximately proportional to $1/f$ as would be expected for $R_s \propto f^2$ (Refs. 13 and 18) since $Q \propto f/R_s$. At high field ($H_{rf} \gg 50$ Oe), the curves merge, indicating that the Q's become independent of f or that $R_s \propto f$. Thus the field $H_p \approx 50$ Oe in Fig. 4 signifies a shift in the frequency dependence of R_s from $R_s \propto f^2$ to $R_s \propto f$. Losses proportional to f^2 are characteristic of quasiparticle conduction losses (see Sec. IV), while losses proportional to f are consistent with hysteresis losses due to vortex penetration.[2] Consequently, we conclude that H_p specifies the vortex-penetration rf field (called H_{c1}^{rf} in Ref. 2) above which magnetic vortices penetrate the bulk of the sample to cause hysteresis losses.

For the rest of this paper, we focus on the region $H_{rf} < H_p$. Analysis of the high-field region will be given in a subsequent publication.

Figure 5 presents a detailed set of R_s vs H_{rf} data at different temperatures for $f_0 = 1.5$ GHz. A least-squares

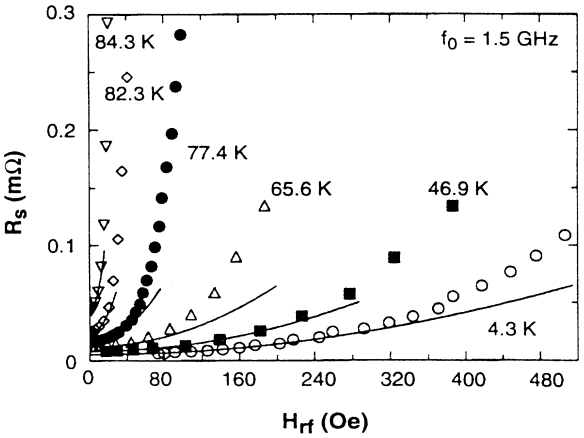

FIG. 5. R_s vs H_{rf} at $f_0 = 1.5$ GHz for resonator 1 at different temperatures. The solid lines are quadratic fits to the data for $H_{rf} < H_p$.

quadratic fit to Eq. (8) is shown at each temperature in each of the intermediate rf field regions. All curves show similar qualitative behavior. Each curve shows that at high fields where $H_{rf} > H_p$, the increase in R_s is faster than H_{rf}^2. The vortex-penetration field H_p decreases with increasing T. For the sake of clarity, the H_p value at each temperature is not explicitly indicated.

Figure 6 shows $\Delta\lambda/\lambda$ vs H_{rf} for the same temperatures as shown in Fig. 5 except that there is no curve at 4.2 K since the change in λ induced by the rf power was smaller than the experimental uncertainties. A least-squares fit of the data to the quadratic form

$$\frac{\Delta\lambda}{\lambda} = b_\lambda H_{rf}^2 \tag{10}$$

is shown for $H_{rf} < H_p$. The functional behavior of $\lambda(H_{rf})$ is similar to that of $R_s(H_{rf})$. The fractional change in λ, however, is very small compared with that of R_s. For

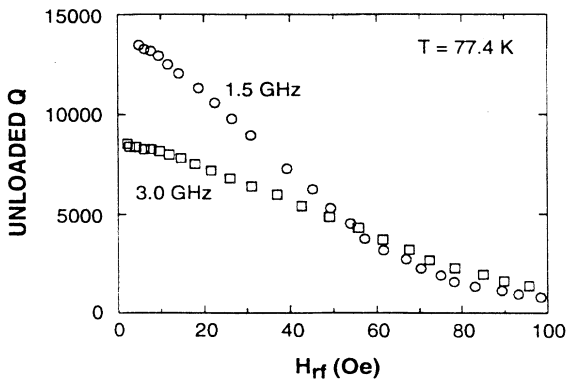

FIG. 4. Q vs H_{rf} for the first two modes ($f_0 = 1.5$ GHz and 3.0 GHz) of resonator 1 at 77 K. The curves merge at high H_{rf}, showing that the frequency dependence of Q and therefore R_s change at high power levels.

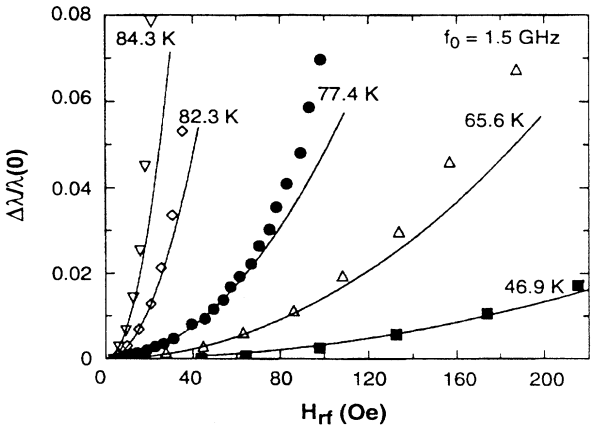

FIG. 6. $\Delta\lambda/\lambda$ vs H_{rf} at $f_0 = 1.5$ GHz for resonator 1 at different temperatures. The solid lines are quadratic fits to the data for $H_{rf} < H_p$.

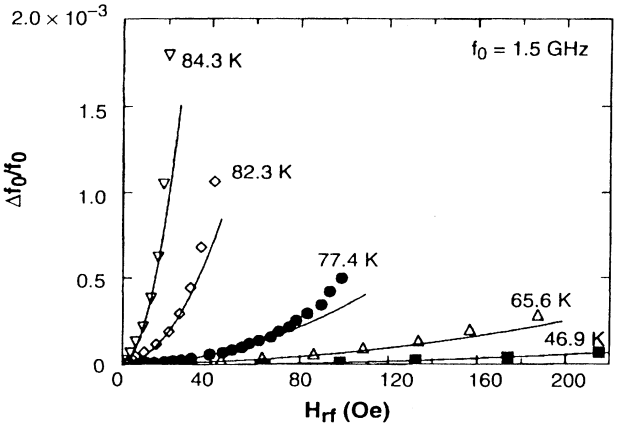

FIG. 7. $\Delta f_0/f_0$ vs $H_{\rm rf}$ at $f_0 = 1.5$ GHz for resonator 1 at the same temperatures as Fig. 6. The solid lines are quadratic fits to the data.

example, $(\Delta\lambda/\lambda) \approx 0.01 \ll (\Delta R_s/R_s) \approx 1.0$ at 79.0 K, 1.5 GHz, and $H_{\rm rf} = 50$ Oe for resonator 1.

Remember that the expression for the effective λ at finite rf power in this paper is only an alternative expression of the resonant frequency of the stripline as defined in Eq. (6). Figure 7 plots the resonant frequencies f_0 as functions of rf field for the same set of temperatures as in Figs. 5 and 6. These resonant frequencies were used to calculate the corresponding effective λ in Fig. 6. The solid curves are quadratic fits to the form $f_0 = f_0(0)(1 - b_f H_{\rm rf}^2)$ where $f_0(0)$ is the zero-field resonant frequency (of that particular mode n) and b_f is the fitting constant.

Figure 8 plots R_s vs $H_{\rm rf}$ at $T = 79.0$ K for several resonant frequencies $n = 1$, 2, 3, and 5 for resonator 1. Mode 4 coincides with and is distorted by a resonant frequency of the package, and hence is not shown here. The fitting procedure is the same as that used in fitting the data in Fig. 5. The vortex-penetration field H_p in Fig. 8 decreases with increasing frequency. For resonators 2 and 3, however, H_p is independent of frequency. We are currently investigating these results for $H_p(f_0)$ to determine the correct relation between H_p and f_0. (The coupled-grain model to be presented in Sec. IV is unaffected by the frequency dependence of H_p.)

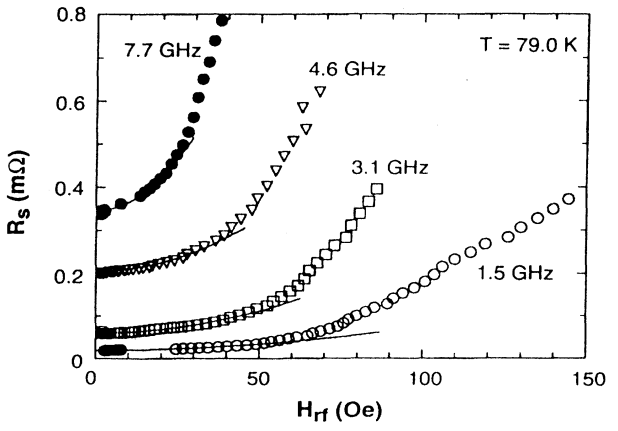

FIG. 8. R_s vs $H_{\rm rf}$ at $T = 79.0$ K for various frequencies for resonator 1. The solid lines are quadratic $H_{\rm rf}^2$ fits to the data.

IV. MODELING

A. Introduction

Various models have been proposed to explain the non-BCS behavior of $R_s(T)$ of the high-temperature superconductors. The coupled-grain model by Hylton *et al.*[8,21] is among the simplest of these models, and it allows for a natural introduction of the rf field dependence. Hylton *et al.*, who considered only the low-field Z_s, modeled the superconductor as a network of superconducting grains coupled via Josephson junctions. The model, however, fails to account quantitatively for the temperature dependence of R_s at low temperature ($t = T/T_c < 0.8$).[8] Attanasio *et al.*[22] extended the coupled-grain model to take into account the field-dependent effects from the grain boundaries.

In this paper, we further developed the coupled-grain concept to simultaneously describe R_s and λ as functions of temperature, frequency, and rf field amplitude. The model accounts for contributions from both the grains and the grain boundaries, resulting in the equivalent circuit for the intra- and intergranular admittances shown in Fig. 9. In the following subsections we derive expressions for the effective complex resistivity of the Y-Ba-Cu-O films. The material is assumed to be composed of identical superconducting grains coupled together by identical intergranular regions, which function as Josephson junctions.

B. Effective complex resistivity

1. *Intragranular resistivity*

For the Y-Ba-Cu-O grains, we apply the anisotropic Ginzburg-Landau (GL) equations[23] with the transport (rf or dc) current density $J(\mathbf{r}, \tau)$ in the ab plane where τ stands for time. We assume isotropy in the ab plane. The frequencies considered in this paper (< 17 GHz) are low enough that the Meissner effect dominates over the classical skin-depth effect and hence the rf current can be treated in the same way as a dc current. Furthermore, that these frequencies are much smaller than $E_g(T)/\hbar >$ 1 THz satisfies the condition for the applicability of the GL equations. Since only the transport currents in the ab plane are considered, the results here are identical to those obtained from solving the usual isotropic GL equations.

Considering the case in which $H_{\rm rf}$ is small enough that the order parameter Ψ varies slowly in space (on the order of the intragranular penetration depth λ_g, which is much larger than the coherence length), we can set $\nabla\Psi = \mathbf{0}$

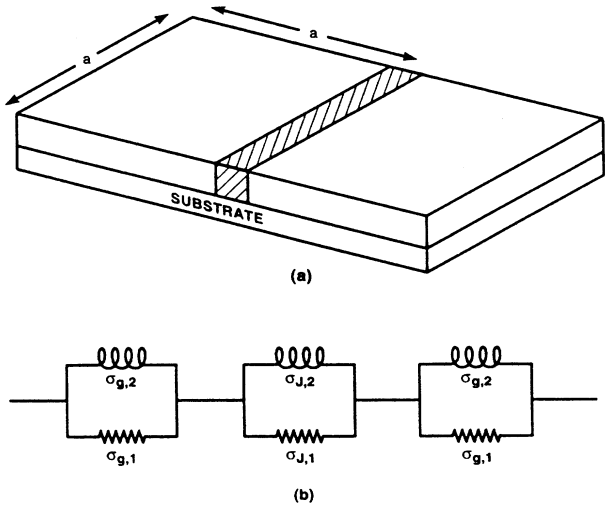

FIG. 9. (a) Two grains of effective grain size a are coupled by a grain boundary which acts as a shunted Josephson junction. One of the two grains and a grain boundary constitute a unit in the coupled-grain model. (b) The equivalent circuit of the unit in (a) with $\sigma_{g,1}$ and $\sigma_{g,2}$ the real and imaginary parts of the conductivity of the grain, and $\sigma_{J,1}$ and $\sigma_{J,2}$ the real and imaginary parts of the grain boundary averaged over the grain size. Note that the shunt resistance R_J is inversely proportional to $\sigma_{J,1}$ and the Josephson junction is represented as purely inductive for low rf currents (much less than the effective critical current of the junction).

and $\nabla^2\Psi = 0$. If we rescale the dimensions so that the anisotropic GL equations become isotropic and use the Coulomb gauge $\nabla \cdot \mathbf{A} = 0$ in the new coordinates, the superconducting electron density n_s as a function of current density can be shown to be

$$\lambda_g^{-2}(T,J) \propto n_s(T,J) = n_s(T,0)[1 - b_0(T)J^2(\mathbf{r},\tau)], \tag{11}$$

where $b_0(T) = \lambda_g^2(T)/2H_c^2(T)$, and H_c and λ_g are the zero-current thermodynamic critical field and intragranular London penetration depth, respectively. At the current densities considered in the low- and intermediate-field regimes, $b_0(T)J^2(\mathbf{r},\tau) \sim 0.01$, assuming $H_c(0\text{ K})$ of the order of 1 T (Ref. 24) and $\lambda_g(0\text{ K}) = 0.15\ \mu$m.[25] Therefore, the shift in n_s or λ can be treated as a perturbation. If we use the temperature dependences $\lambda_g \propto 1/(1-t^4)^{1/2}$ and $H_c \propto (1-t^2)$ from the two-fluid model, then

$$b_0(T) = \frac{\lambda_g^2(0\text{ K})}{2H_c^2(0\text{ K})}\frac{1}{(1-t^4)(1-t^2)^2}. \tag{12}$$

Assuming that the real part $\sigma_{g,1}$ of the intragranular conductivity $\sigma_g = \sigma_{g,1} - j\sigma_{g,2}$ is much smaller than the imaginary part $\sigma_{g,2}$, we get the usual two-fluid model resistivity $\rho_g = \rho_{g,1} + j\rho_{g,2}$,[26] where

$$\rho_{g,1} = \frac{\sigma_{g,1}}{\sigma_{g,2}^2} \tag{13}$$

and

$$\rho_{g,2} = \omega\mu_0\lambda_g^2(T,J) \tag{14}$$

with

$$\lambda_g^2(T,J) = \lambda_g^2(0\text{ K})[1 + b_0(T)J^2(\mathbf{r},\tau)]\frac{1}{(1-t^4)}. \tag{15}$$

Note from Eq. (13) that $\sigma_{g,1}$ and hence $\rho_{g,1}$ go to zero as $T \to 0$ (see Ref. 26).

2. *Intergranular resistivity*

The intergranular resistivity is derived assuming the grains are connected by resistively shunted Josephson junctions[22] of effective critical current density J_c. For $J \ll J_c$, at the frequencies considered here, the inductive impedance dominates the resistive impedance (see Fig. 9). The real and imaginary parts of the effective resistivity $\rho_J = \rho_{J,1} + j\rho_{J,2}$, averaged over the cubic grains of size a, are derived in Refs. 8 and 22 and rewritten keeping only the lowest-order terms in J ($\ll J_c$),

$$\rho_{J,1} = \frac{\omega^2\mu_0\lambda_J^2(T)\hbar}{2eJ_c(T)R_J}A\left(1 + \frac{J^2(\mathbf{r},\tau)}{J_c^2(T)}\right) \tag{16}$$

and

$$\rho_{J,2} = \omega\mu_0\lambda_J^2(T)\left(1 + \frac{J^2(\mathbf{r},\tau)}{2J_c^2(T)}\right), \tag{17}$$

where the effective continuum penetration depth λ_J is defined as

$$\lambda_J(T,J) \equiv \left(\frac{\hbar}{2eaJ_c(T)\mu_0}\left[1 - \frac{J^2(\mathbf{r},\tau)}{J_c^2(T)}\right]\right)^{1/2}. \tag{18}$$

R_J is the (temperature-independent) shunt resistance of the Josephson junctions and the junction cross-sectional area $A = a^2$ or ad for grain size a smaller or larger than film thickness d, respectively. The effective continuum penetration depth λ_J should not be confused with the Josephson penetration depth which considers the details of the penetration in the junction region even though the two resemble each other in form (in the limit of zero rf power $J \to 0$).[8] The explicit power dependences in Eqs. (16) and (17) arise from the power dependence of the inductance of the Josephson junction.[22] We have dealt explicitly with the nonuniform current distribution $J(\mathbf{r},\tau)$, which is assumed to be the same as that for a superconducting stripline with no grain boundaries. (This assumption is valid since our films are in the large-grain and strong-coupling regime,[27] as we see in Sec. V.) Consequently, our results, which are derived for short junctions, can be generalized easily to long junctions by integrating over the whole junction area, assuming a uniform J_c across each junction.

3. Total resistivity

The total effective complex resistivity $\rho = \rho_1 + j\rho_2$ is the sum of the intra- and intergranular resistivities, ρ_g and ρ_J, respectively, where

$$\rho_1 = \rho_{g,1} + \rho_{J,1} \tag{19}$$

and

$$\rho_2 = \rho_{g,2} + \rho_{J,2} = \omega\mu_0\lambda^2(T,J), \tag{20}$$

with

$$\lambda^2(T,J) = \lambda_g^2(T,J) + \lambda_J^2(T,J). \tag{21}$$

From Eq. (16), we obtain

$$\rho_1(f,T,J) = \rho_1(f,T,0)(1 + b_\rho J^2), \tag{22}$$

with

$$b_\rho = b_{\rho,g} + b_{\rho,J} \tag{23}$$

where

$$b_{\rho,g} = \frac{2[1 - n_s(T,0)/2]b_0(T)}{[1 - n_s(T,0)]} \frac{\rho_{g,1}(f,T,0)}{\rho_1(f,T,0)} \tag{24}$$

is the intragranular contribution and

$$b_{\rho,J} = \frac{1}{J_c^2(T)} \frac{\rho_{J,1}(f,T,0)}{\rho_1(f,T,0)} \tag{25}$$

is the intergranular contribution. From Eqs. (14) and (17), we write

$$\rho_2 \propto \lambda^2(T,J) = \lambda^2(T)(1 + b_\lambda J^2), \tag{26}$$

with

$$b_\lambda = b_{\lambda,g} + b_{\lambda,J}, \tag{27}$$

where

$$b_{\lambda,g} = 2b_0(T)\frac{\lambda_g^2(T)}{\lambda^2(T)} \tag{28}$$

is the intragranular contribution and

$$b_{\lambda,J} = \frac{1}{2J_c^2(T)} \frac{\lambda_J^2(T)}{\lambda^2(T)} \tag{29}$$

is the intergranular contribution.

C. Zero rf field limit

The surface impedance Z_s can be calculated from the formula for the surface impedance of a good conductor $Z_s = (j\omega\mu_0\rho)^{1/2}$, where ρ is the total effective resistivity derived above. Since $\rho_2 \gg \rho_1$,[28]

$$Z_s = R_s + jX_s \approx \frac{\rho_1}{2\lambda} + j\omega\mu_0\lambda, \tag{30}$$

where $\lambda^2 = \lambda_g^2 + \lambda_J^2$ [see Eq. (21)]. Equation (30) in the limit of zero rf field is similar in form to that derived by Hylton *et al.*,[8] except that ρ_1 here includes both the intra- and intergranular contributions [see Eq. (19)].

D. rf field dependence

We estimate the power dependence of Q and the resonant frequency f_0 (of some mode n) for $H_{\rm rf} < H_p$. Since the center conductor is much narrower and its peak current density is at least 2 orders of magnitude larger than that in the ground planes,[11,14] the contribution to the surface impedance from the ground planes is more than an order of magnitude smaller and hence will be neglected. The power loss P of the stripline resonator, averaged over one cycle, is given by

$$P = \int_0^{1/f_0} \frac{d\tau}{(1/f_0)} \int_0^l dz \int_A \rho_1(f_0,T,J)J^2(\mathbf{r},\tau)dx\,dy, \tag{31}$$

where A is the cross-sectional area of the center conductor and $J(\mathbf{r},\tau)$ is the current density flowing in the z direction (along the stripline of length l) as calculated in Ref. 14. From Eq. (2),

$$J(\mathbf{r},\tau) = J_0(x,y)\sin\left(\frac{n\pi}{l}z\right)\cos(\omega_0\tau), \tag{32}$$

where $\int_A J_0(x,y)dx\,dy = I_0$ and $\omega_0 \equiv 2\pi f_0$. We have assumed that the current distribution remains unaffected by a change in the rf power. This assumption is good in the low- and intermediate-field regimes ($H_{\rm rf} < H_p$) since the change in λ, which determines the current distribution, is small relative to λ as discussed above in Sec. III B. Substituting Eq. (22) into Eq. (31) and integrating over τ and z, we obtain

$$P(I_0) = P(0)\left(1 + \frac{9b_\rho}{16}GI_0^2\right), \tag{33}$$

where

$$G = \frac{\int_A J_0^4 dx\,dy}{\int_A J_0^2 dx\,dy(\int_A J_0 dx\,dy)^2} \tag{34}$$

and

$$P(0) \equiv \frac{l}{4}\int_A \rho_1(f_0,T,0)J_0^2 dx\,dy. \tag{35}$$

The factor G in Eq. (34) is determined by the cross-sectional current distribution which depends on the geometry of the transmission line.

The total stored energy E averaged over one cycle in the stripline resonator can be expressed through the inductive part of the circuit: $E = E_m + E_k$, where E_m is the stored magnetic energy and E_k the stored supercurrent kinetic energy (giving rise to the kinetic inductance). More specifically,

$$E_m = \int_0^{1/f_0} \frac{d\tau}{(1/f_0)} \int_V \mu_0|\mathbf{H}(\mathbf{r},\tau)|^2 d\mathbf{r} \tag{36}$$

and

$$E_k = \int_0^{1/f_0} \frac{d\tau}{(1/f_0)} \int_0^l dz \int_A \mu_0 \lambda^2(T,J) J^2(\mathbf{r},\tau) dx\, dy, \tag{37}$$

where V is the total volume of the stripline resonator and $\mathbf{H}(\mathbf{r},\tau)$ the rf magnetic field. The total inductance L, the magnetic inductance L_m, and the kinetic inductance L_k of the resonator can be obtained from $\frac{1}{4}LI_0^2 = E$, $\frac{1}{4}L_mI_0^2 = E_m$, and $\frac{1}{4}L_kI_0^2 = E_k$, respectively. Since the current distribution is basically unaltered by a change in the rf power as discussed before, increasing the rf power, or equivalently the rf field, produces little change in L_m. Consequently, we can attribute all of the power dependence of L to L_k. (Direct numerical calculations of the kinetic inductance and the internal and external inductances confirmed the domination in power dependence of the kinetic inductance.[14]) Since $\Delta f_0/f_0 = -\Delta L/2L$, from Eq. (37), after a few simple integrations, we get

$$f_0(H_{\rm rf}) = f_0(0)(1 - b_f H_{\rm rf}^2), \tag{38}$$

in which the quadratic coefficient b_f, that depends on T, is given by

$$b_f = -\frac{\Delta f_0}{f_0 I_0^2} C \approx \frac{1}{2}\left(\frac{L_k(H_{\rm rf}=0)}{L(H_{\rm rf}=0)}\right)\left(\frac{9b_\lambda}{16}\right)GC, \tag{39}$$

where $\Delta f_0 \equiv f_0(H_{\rm rf}) - f_0(0)$ and $C = C(T)$ is the proportionality constant between I_0^2 and $H_{\rm rf}^2$ in the limit $I_0 = 0$, i.e., $I_0^2 = CH_{\rm rf}^2$.

Similarly, we can write

$$Q = \frac{\omega E}{P} \approx \frac{\omega E(H_{\rm rf}=0)}{P(H_{\rm rf}=0)}\left(1 - \frac{9b_\rho}{16} G I_0^2\right). \tag{40}$$

Since $R_s \propto 1/Q$, we obtain an expression for the quadratic coefficient $b_R(T)$ [defined in Eq. (8)]:

$$b_R = \frac{\Delta R_s}{R_s(H_{\rm rf}=0) I_0^2} C \approx \frac{9b_\rho}{16} GC, \tag{41}$$

where $\Delta R_s = R_s(H_{\rm rf}) - R_s(0)$.

V. COMPARISON BETWEEN MODEL AND EXPERIMENT

The real part $\rho_{g,1}$ of the intragranular resistivity approaches zero exponentially for $t < 0.7$ in both the BCS theory and the two-fluid model [Eq. (13)]. In contrast, the imaginary part $\rho_{g,2} \propto \lambda$ approaches a finite value at $T = 0$. Consequently, we expect the introduction of the grain boundaries to produce a large increase in R_s but only a relatively small shift in X_s. In fact, the intergranular contribution to X_s becomes significant only when there are enough "bad" grain boundaries (of low junction critical currents), or more quantitatively, when $\lambda_J \geq \lambda_g$. We will see below that R_s and its field dependence are dominated by the grain boundaries, whereas the magnitude of λ is dominated by the grains. The field dependence of λ, however, is dominated by the grain boundaries.

There are three fitting parameters, $J_c(T)$, a, and R_J, that need to be determined in the coupled-grain model. Since the power dependence of $R_s(T)$ and $X_s(T)$ are most sensitive to $J_c(T)$ and a, respectively, we will start by comparing the calculated $b_R(T)$ and $b_f(T)$ with the measurements. The extracted values of $J_c(T)$ and a will then be used in estimating the zero field $R_s(T)$ using R_J as a fitting parameter.

A. rf field dependence

The rf field dependence of R_s and λ in the low- and intermediate-field range is characterized by the quadratic coefficients $b_R(T)$ and $b_f(T)$ defined in Eqs. (8) and (38), respectively. To estimate $b_R(T)$ and $b_f(T)$ from Eqs. (41) and (39), respectively, we calculate the geometrical factor $G(T)$ from Eq. (34), the proportionality constant $C(T)$ in $I_0^2 = CH_{\rm rf}^2$, and the ratio $L_k(H_{\rm rf}=0,T)/L(H_{\rm rf}=0,T)$, using the current distributions derived numerically by Sheen *et al.*[14]

1. Surface resistance

For the junction critical current density $J_c(0\ {\rm K})$ between 10^6 and 10^7 A/cm^2, the power dependence of R_s (or the unloaded Q) from the grain boundaries is much larger than that from the grains, i.e., $b_{\rho,g} \ll b_{\rho,J}$, assuming $H_c(0\ {\rm K})$ of the order of 1 T (Ref. 24) and $\lambda_g = 0.15\ \mu$m (Ref. 25) as before. From Eqs. (23) and (25), we can write

$$b_\rho \approx b_{\rho,J} \approx \frac{1}{J_c^2(T)} \tag{42}$$

throughout the entire temperature range below T_c. Hence, from Eq. (41), we get

$$b_R \approx \frac{9b_{\rho,J}}{16} GC. \tag{43}$$

Figure 10 plots b_R derived from the data used in Fig. 5 as a function of temperature. The solid line is the calculated b_R from Eq. (43) using $a = 3.5\ \mu$m (as derived in the next subsection), $\lambda_g(T) = \lambda_g(0)/\sqrt{1-(T/T_c)^4}$, and the Ambegaokar form for the junction critical current density

$$J_c(T) = J_c(0)\frac{E_g(T)}{E_g(0)} \tanh \frac{E_g(T)}{2k_BT}, \tag{44}$$

where $J_c(0) = \pi E_g(0)/2eAR_n$, and R_n is the quasiparticle-tunneling resistance (different from the shunt resistance R_J of the weak link). The critical current density $J_c(0)$ is a fitting parameter [to $b_R(T)$]. (Instead of J_c, we could have equally picked R_n to be the

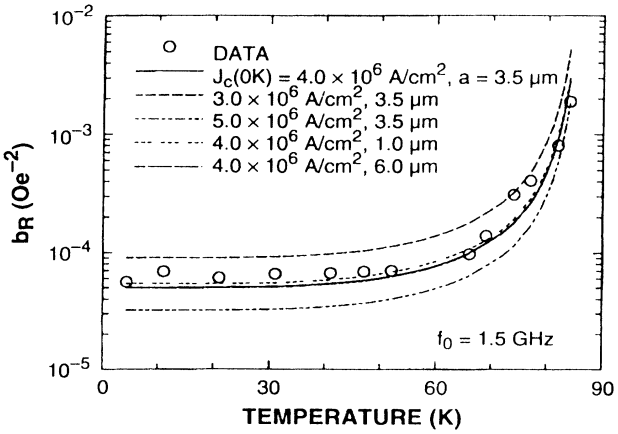

FIG. 10. Temperature dependence of the quadratic coefficient b_R. The solid line is calculated from the coupled-grain model using the first set of values from Table II. The dashed lines are produced by the remaining four sets of values from the same table.

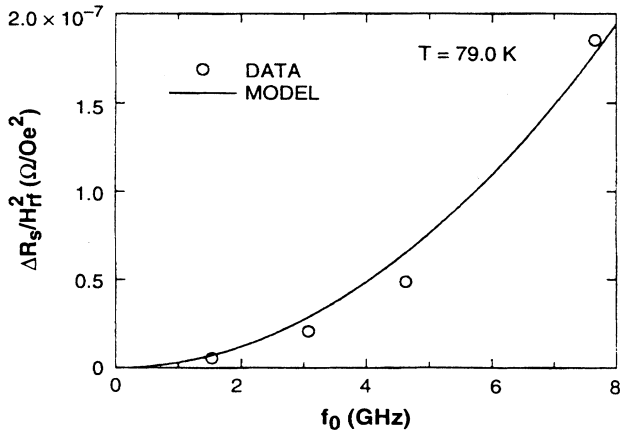

FIG. 11. Frequency dependence of $\Delta R_s/H_{rf}^2$. The solid line is the best least-squares fit of the data to $C_R f^2$ with C_R a fitting parameter.

fitting parameter since $J_c \propto R_n$.) The energy gap $E_g(T)$ is assumed to follow the BCS temperature dependence and $2E_g(0)/k_BT_c = 4.3$ as used by Sridhar *et al.*[29] to fit their $R_s(T)$ data. As seen in Fig. 10, the agreement of the temperature dependence between the calculated curve (solid line) and the measurements is good over the entire temperature range. Furthermore, the value of $J_c(0) \approx 4.0 \times 10^6$ A/cm^2 obtained is comparable to the transport critical current densities $J_c^T(0)$ of the samples (see Table I).

The dashed lines in Fig. 10 are estimates of b_R with slight variations of a and $J_c(0)$ to show the sensitivity of the calculations to these two fitting parameters (see Table II). The shunt resistance R_J has been modified correspondingly to yield the same zero field $R_s(T)$. Note that R_J affects only the zero field $R_s(T)$ (and not b_R or b_f), and b_R is far more sensitive to J_c than to a.

Figure 11 shows $\Delta R_s/H_{rf}^2 \equiv [R_s(H_{rf}) - R_s(0)]/H_{rf}^2 = R_s(0)b_R$ as a function of frequency. Since b_R is independent of f [Eq. (43)] and $R_s(0) \propto f^2$ (Ref. 18), $\Delta R_s/H_{rf}^2$ is proportional to f^2. This quadratic dependence on f is observed experimentally in Fig. 11, where the solid line (through the origin) is the best least-squares quadratic fit to $C_R f^2$. The fitting parameter C_R agrees within the experimental error with the calculation using the best calculated b_R and the experimentally determined value of $R_s(H_{rf} = 0)$.

TABLE II. Fitting parameters from the coupled-grain model for the $YBa_2Cu_3O_{7-x}$ films discussed in the text. Sets 2 through 5 for film 1 are chosen to give the same zero field $R_s(T)$.

Film (set)	$J_c(0\text{ K})$ (A/cm^2)	a (μm)	R_J (mΩ)
1 (1)[a]	4.0×10^6	3.5	0.09
1 (2)	3.0×10^6	3.5	0.16
1 (3)	5.0×10^6	3.5	0.06
1 (4)	4.0×10^6	1.0	3.60
1 (5)	4.0×10^6	6.0	0.02
2	3.4×10^6	3.0	0.01
3	2.1×10^6	3.0	0.32

[a]Best set.

2. *Effective penetration depth*

With $H_c(0\text{ K})$ of the order of 1 T (Ref. 24), we find from Eqs. (18), (28), and (29) that $b_{\lambda,J}(T) \gg b_{\lambda,g}(T)$ even though $\lambda_J(T) < \lambda_g(T)$. In other words, the effective penetration depth λ is determined by the grains but its power dependence is governed by the grain boundaries. Figure 12 presents the measured b_f as a function of T. The solid line is the calculated b_f from Eq. (39)

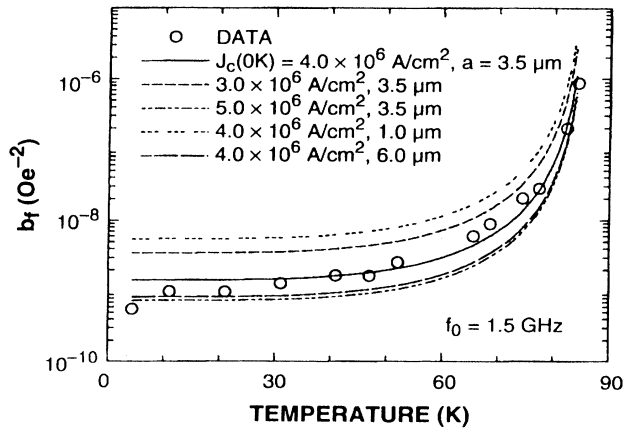

FIG. 12. Temperature dependence of the quadratic coefficient b_f. The solid line is calculated from the coupled-grain model using the first set of values from Table II. The dashed lines are produced by the remaining four sets of values from the same table.

using the value $J_c(0) = 4.0 \times 10^6$ A/cm^2 obtained above, and a as an adjustable parameter whose value $a = 3.5$ μm (also used previously) gives a close fit to the data. The agreement between the calculated $b_f(T)$ and the measurements is good. The *effective* grain size a is much larger than the average grain sizes [typically less than 1 μm (Refs. 21, 30, and 31)] probably because it denotes the average distance between only the grain boundaries with low critical current densities which are important in determining the power dependence of λ.

The dashed curves in Fig. 12, which are calculated from the remaining four sets of parameters in Table II, are also presented to show the sensitivity of the calculated b_f to variations of the corresponding fitting parameters a and J_c. It can be seen that b_f is nearly equally sensitive to variations of both $J_c(0\ \mathrm{K})$ and a.

Figure 13 plots $\Delta f_0/H_{\mathrm{rf}}^2 = [f_0(I_0) - f_0(0)]/H_{\mathrm{rf}}^2 = f_0(0)b_f$ vs frequency. From the model, $\Delta f_0/H_{\mathrm{rf}}^2 \propto f$ for the frequency range considered in this paper ($f_0 < 17$ GHz), since b_f is independent of f [Eqs. (29) and (39)]. This linear dependence of the calculated $\Delta f_0/H_{\mathrm{rf}}^2$ on f is consistent with the measurement as seen by the straight line fit in Fig. 13 (solid line) to $C_f f$, where the fitting parameter C_f agrees within the experimental error with the calculation using the best calculated b_f and the experimentally determined $f_0(H_{\mathrm{rf}} = 0)$.

B. Zero rf field limit

The surface resistance R_s falls rapidly below T_c in both the two-fluid model and the BCS theory. The dashed curve in Fig. 14 shows a BCS calculation for R_s as a function of the reduced temperature t (Ref. 32) with $2E_g(0\ \mathrm{K})/k_BT_c = 4.3$, coherence length $\xi_0 = 3.1$ nm, and mean free path $l_0 = 7.0$ nm as in Ref. 29, and $\lambda_g(0\ \mathrm{K}) = 0.15$ μm as before. Above $t \approx 0.9$, the R_s values derived from our data drop more rapidly than predicted by the BCS model. This sharp superconducting transition has been observed also in Y-Ba-Cu-O single crystals.[20] The behavior of R_s at low temperature is clearly non-BCS. By the coupled-grain model considered here, the high residual value for R_s below $t = 0.9$ must come from the grain boundaries. From Eq. (30), neglecting $\rho_{g,1}$ and letting $\rho_1 = \rho_{J,1}$ for $t < 0.9$ where $\rho_{J,1}$ can be estimated from Eq. (16), we obtain the following relation for R_s in the $H_{\mathrm{rf}} \to 0$ limit:

$$R_s(f,T,0) = \frac{\rho_{J,1}(f,T,0)}{2\lambda(T,0)}. \tag{45}$$

By using the $J_c(T)$ and a derived in Sec. V A (set 1 for film 1 in Table II), a least-squares fit of Eq. (45) to the R_s data gives $R_J = 0.09$ mΩ. The fit (solid line in Fig. 14) looks reasonable especially at low temperature ($t < 0.3$), though improvements to the fit close to T_c can be made if we introduce a temperature dependence to the *effective* R_J.

The value of R_J obtained here is about 3 orders of magnitude smaller than that measured by Gross *et al.*[33] and Chaudhari *et al.*[34] on fabricated grain-boundary single junctions. The difference in R_J may be due to two factors: the critical current densities of the fabricated grain boundaries in Refs. 33 and 34 are an order of magnitude smaller than those for our films, and our effective grain size a is large. From Eq. (45), the fitting parameter R_J goes as $R_J \sim J_c^{-2}$ keeping everything else constant. Our larger critical current densities, therefore, should account for most of the difference between our value of R_J and those measured from fabricated grain-boundary junctions.[33,34] Moreover, since the fitting parameter R_J also goes as $R_J \sim a^{-3}$ [Eq. (45)] keeping everything else constant, our large effective grain size a should account for the rest of the difference.

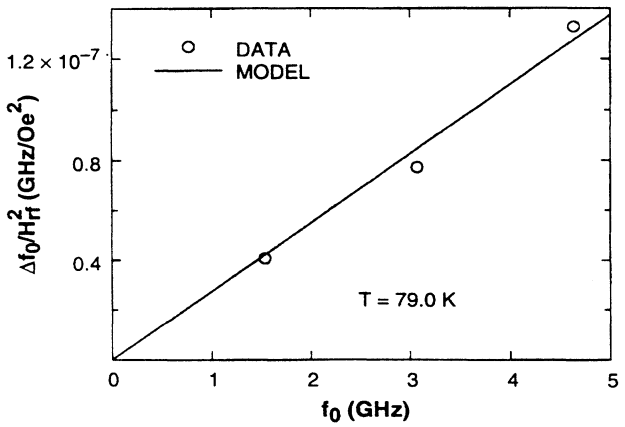

FIG. 13. Frequency dependence of $\Delta f_0/H_{\mathrm{rf}}^2$. The solid line is the best least-squares fit of the data to $C_f f$ with C_f a fitting parameter.

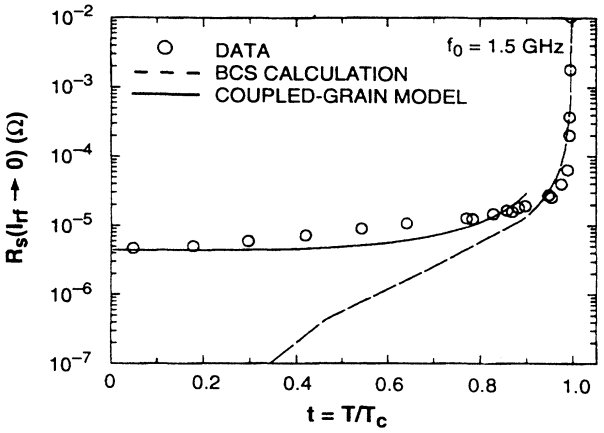

FIG. 14. Zero field R_s for resonator 1 (circles). The dashed line is a BCS calculation with $\lambda(T = 0, H_{\mathrm{rf}} = 0) = 0.15$ μm, $2E_g(0\ \mathrm{K})/k_BT_c = 4.3$, coherence length $\xi_0 = 3.1$ nm, and mean free path $l_0 = 7.0$ nm. The solid line is a calculation from the coupled-grain model as discussed in the text.

C. Vortex-penetration field H_p

Figure 15 shows H_p vs T for resonator 1 at 1.5 GHz. The long-dashed curve is the best least-squares fit

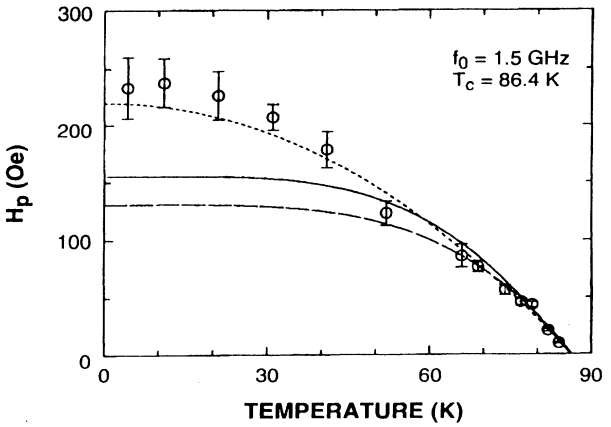

FIG. 15. Vortex-penetration field $H_p(T)$ vs temperature for resonator 1 at 1.5 GHz. The long-dashed line is the best fit to $H_p(0\text{ K})[1-(T/T_c)^4]$ with $H_p(0\text{ K})$ a fitting parameter. The solid line is the best fit to the function $H_p = C_H J_c(T)$ where $J_c(T)$ is given by Eq. (44) and C_H is a fitting parameter. The short-dashed line is the best fit to the function $H_p = H_p(0\text{ K})[1-(T/T_c)^2]$ as suggested in Ref. 3.

(weighted by the error) to the two-fluid model functional form for the dc lower critical field $H_p(0\text{ K})[1-(T/T_c)^4]$ where $H_p(0\text{ K})$ is a fitting constant. The fit becomes very poor below about 60 K, where the experimental points also have larger error bars because of the gradual deviation of R_s from a quadratic dependence of R_s on $H_{\rm rf}$ at low temperatures. Because vortices first enter the grain boundaries (where superconductivity is weakened) rather than the grains, H_p is more likely to reflect the lower critical field $H_{c1,J}$ of the grain boundaries. Since $H_{c1,J}$ is directly proportional to $J_c(T)$,[35,36] the temperature dependence of $H_{c1,J}$ should follow approximately that of the J_c of a Josephson junction. The solid line in Fig. 15 is the best least-squares fit to $H_p = C_H J_c(T)$ where $J_c(T)$ is given by Eq. (44) and the proportionality constant C_H is a fitting parameter relating $H_{c1,J}(T)$ to $J_c(T)$. The results in Fig. 15 show that the fit of the experimental points to the Ambegaokar critical current function is slightly better than that to the two-fluid model but still well outside the experimental error.

If we use the functional form suggested in Ref. 3, $H_p = H_p(0\text{ K})[1-(T/T_c)^2]$ with $H_p(0\text{ K})$ as a fitting parameter, the fit becomes excellent (short-dashed curve in Fig. 15). This functional form for the vortex-penetration field, however, is not well justified theoretically.

VI. SUMMARY

We have presented a detailed characterization of $Z_s(T, f, H_{\rm rf})$ for high-quality films of $YBa_2Cu_3O_{7-x}$ deposited *in situ* on $LaAlO_3$ by off-axis sputtering. For small $H_{\rm rf}$, we find that for reduced temperature $t < 0.5$, the real part of Z_s, i.e., R_s, differs from the BCS theory by orders of magnitude. With an appropriate set of characteristic parameters — J_c, a, and R_J — we have simultaneously accounted for the behavior of the zero field R_s and the rf field dependence of both R_s and λ as functions of temperature and frequency, using a coupled-grain model in which the superconductor is modeled as a network of superconducting grains of intrinsic properties connected by weak-link Josephson junctions whose properties are extrinsic to the fundamental material and depend on film deposition and sample preparation.

It is interesting to note that the fractional power-induced change in R_s is more than 100 times larger than the fractional change in λ. This is explained by the coupled-grain model in a simple way. The resistance is dominated by the properties of the weak-link Josephson junctions, which show a strong dependence on rf magnetic field. The zero-field inductance is dominated by the intrinsic properties of the grains, which have weak dependencies on the rf field. As the rf field is increased, the intergranular inductance increases much more rapidly than the intragranular inductance. The change in the intergranular inductance, however, is moderated by the large zero-field intragranular inductance.

The field H_p signifies the onset of vortex penetration into the grain boundaries. The behavior of R_s and λ in the high-field region $H_{\rm rf} > H_p$ has not yet been modeled in detail. This will be the subject of further investigation. We have identified the field H_p as the field at which the penetration of vortices becomes important. As discussed earlier, there is a change in the frequency dependence of the surface resistance above H_p. In the limit of zero rf field, R_s is proportional to f^2, as would be expected for losses dominated by quasiparticles. For larger fields, R_s becomes proportional to f, which is consistent with hysteresis losses resulting from flux penetration.

Work is currently under way to describe the rf field dependence in the region where rf vortices are present. We also plan to study the frequency dependence of H_p since our measurements on $H_p(f)$ to date are inconclusive with regard to the frequency dependence. The data of Fig. 6 indicate that H_p decreases with frequency; however, other samples have shown that H_p can be independent of f (see Fig. 7). The vortex-penetration field $H_p(T)$ is not described well by either the BCS or the Ambegaokar expression. This will also be investigated further.

ACKNOWLEDGMENTS

At MIT Lincoln Laboratory, the work was supported in part by the Department of the Air Force and in part by the Defense Advanced Research Projects Agency under the auspices of the Consortium for Superconducting Electronics. The work of G.O. at the Rome Laboratory was supported by the University Research Resident Program of the Air Force Office of Scientific Research. We wish to thank R. P. Konieczka for help with the measurements, G. Fitch for programming, and A. C. Anderson of MIT Lincoln Laboratory and N. Newman of Conductus Inc. for supplying the high-T_c films. We also gratefully acknowledge numerous technical discussions with and suggestions from Dr. J. Halbritter.

[1] H. Piel, H. Chaloupka, and G. Müller, in *Advances in Superconductivity IV* (Springer-Verlag, Tokyo, 1992).
[2] D. E. Oates, P. P. Nguyen, G. Dresselhaus, M. S. Dresselhaus, C. W. Lam, and S. M. Ali, J. Supercond. **5**, 361 (1992).
[3] A. A. Valenzuela, G. Sölkner, J. Kessler, and P. Russer, in *High Temperature Superconductors*, Materials Science Forum, edited by J. J. Pauch, S. A. Alterovitz, and R. R. Romanofsky (Trans Tech, Aedermannsdorf, Switzerland, 1992).
[4] J. R. Delayen and C. L. Bohn, Phys. Rev. B **40**, 5151 (1989).
[5] J. Halbritter, J. Appl. Phys. **68**, 6315 (1990).
[6] J. Halbritter, Supercond. Sci. Technol. **4**, 127 (1991).
[7] J. Halbritter, J. Supercond. **5**, 171 (1992).
[8] T. L. Hylton, A. Kapitulnik, M. R. Beasley, J. P. Carini, L. Drabeck, and G. Grüner, Appl. Phys. Lett. **53**, 1343 (1988).
[9] K. Scharnberg and D. Walker, J. Supercond. **3**, 269 (1990).
[10] W. Rauch, E. Gornik, G. Sölkner, A. A. Valenzuela, F. Fox, and H. Behner, J. Appl. Phys. **73**, 1866 (1993).
[11] C. W. Lam, D. M. Sheen, S. M. Ali, and D. E. Oates, IEEE Trans. Appl. Supercond. **2**, 58 (1992).
[12] C. W. Lam, S. M. Ali, and D. E. Oates (unpublished).
[13] D. E. Oates, A. C. Anderson, D. M. Sheen, and S. M. Ali, IEEE Trans. Microwave Theory Tech. **39**, 1522 (1991).
[14] D. M. Sheen, S. M. Ali, D. E. Oates, R. S. Withers, and J. A. Kong, IEEE Trans. Appl. Supercond. **1**, 108 (1991).
[15] A. S. Westerheim, L. S. Yu-Jahnes, and A. C. Anderson, IEEE Trans. Magn. **27**, 1001 (1991).
[16] A. M. Portis, D. W. Cooke, and E. R. Gray, J. Supercond. **3**, 297 (1990).
[17] J. H. Oates, R. T. Shin, D. E. Oates, M. J. Tsuk, and P. P. Nguyen, IEEE Trans. Appl. Supercond. **3**, 17 (1993).
[18] D. E. Oates, A. C. Anderson, and P. M. Mankiewich, J. Supercond. **3**, 251 (1990).
[19] S. M. Anlage, B. W. Langley, G. Deutscher, J. Halbritter, and M. R. Beasley, Phys. Rev. B **44**, 9764 (1991).
[20] D. A. Bonn, P. Dosanjh, R. Lang, and W. N. Hardy, Phys. Rev. Lett. **68**, 2390 (1992).
[21] T. L. Hylton and M. R. Beasley, Phys. Rev. B **39**, 9042 (1989).
[22] C. Attanasio, L. Mariato, and R. Vaglio, Phys. Rev. B **43**, 6128 (1991).
[23] T. P. Orlando and K. A. Delin, *Foundations of Applied Superconductivity* (Addison-Wesley, Reading, MA, 1991).
[24] Dong-Ho Wu and S. Sridhar, Phys. Rev. Lett. **65**, 2074 (1990).
[25] D. R. Harshman, G. Aeppli, E. J. Ansaldo, B. Batlogg, J. H. Brewer, J. F. Carolan, R. J. Cava, M. Celio, A. C. D. Chaklader, W. N. Hardy, S. R. Kreitzman, G. M. Luke, D. R. Noakes, and M. Senba, Phys. Rev. B **36**, 2386 (1987).
[26] T. van Duzer and C. W. Turner, *Principles of Superconductive Devices and Circuits* (Elsevier-North-Holland, New York, 1981).
[27] T. L. Hylton, Ph.D. thesis, Department of Physics, Stanford University, 1991.
[28] N. Klein, U. Poppe, N. Tellmann, H. Schulz, W. Evers, U. Dähne, and K. Urban, IEEE Trans. Appl. Supercond. **3**, 1102 (1993).
[29] S. Sridhar, Dong-Ho Wu, and W. Kennedy, Phys. Rev. Lett. **63**, 1873 (1989).
[30] C. B. Eom, J. Z. Sun, K. Yamamoto, A. F. Marshall, K. E. Luther, S. S. Laderman, and T. H. Geballe, Appl. Phys. Lett. **55**, 595 (1989).
[31] C. B. Eom, J. Z. Sun, B. M. Lairson, S. K. Streiffer, A. F. Marshall, K. Yamamoto, S. M. Anlage, J. C. Bravman, and T. H. Geballe, Physica C **171**, 354 (1990).
[32] J. Halbritter, Z. Phys. **266**, 209 (1974).
[33] R. Gross, P. Chaudhari, M. Kawasaki, and A. Gupta, Phys. Rev. B **42**, 10735 (1990).
[34] P. Chaudhari, J. Mannhart, D. Dimos, C. C. Tsuei, J. Chi, M. M. Oprysko, and M. Scheuermann, Phys. Rev. Lett. **60**, 1653 (1988).
[35] J. R. Clem, Physica C **153**, 50 (1988).
[36] M. Tinkham and C. J. Lobb, Solid State Phys. **42**, 91 (1989).